Using pH dependence to understand mechanisms in electrochemical CO reduction

Georg Kastlunger[a], Lei Wang[b,c], Nitish Govindarajan[a], Hendrik H. Heenen[a], Stefan Ringe[d,e], Thomas Jaramillo[b], Christopher Hahn[f,g], Karen Chan[a,*]

[a]Catalysis Theory Center, Department of Physics, Technical University of Denmark (DTU), 2800 Kgs. Lyngby, Denmark
[b]SUNCAT Center for Interface Science and Catalysis, Department of Chemical Engineering, Stanford University, Stanford, CA 94305, USA
[c]Department of Chemical and Biomolecular Engineering, National University of Singapore, Singapore 117585, Singapore
[d]Department of Energy Science and Engineering, Daegu Gyeongbuk Institute of Science and Technology, Daegu, Republic of Korea
Energy Science and Engineering Research Center, Daegu Gyeongbuk Institute of Science and Technology (DGIST), Daegu 42988, Republic of Korea
[f]SUNCAT Center for Interface Science and Catalysis, SLAC National Accelerator Laboratory, Menlo Park, CA 94025, USA
[g]Materials Science Division, Lawrence Livermore National Laboratory, Livermore, CA 94550, USA

Electrochemical conversion of $CO_{(2)}$ into hydrocarbons and oxygenates is envisioned as a promising path towards closing the carbon cycle in modern technology. To this day, however, the reaction mechanisms towards the plethora of products are disputed, complicating the search for novel catalyst materials. In order to conclusively identify the rate-limiting steps in CO reduction on Cu, we analyzed the mechanisms on the basis of constant potential DFT calculations and experiments at a wide range of pH values (3 - 13). We find that *CO dimerization is energetically favoured as the rate limiting step towards multi-carbon products. This finding is consistent with experiments, where the reaction rate is nearly unchanged on an SHE potential scale, even under acidic conditions. For methane, both theory and experiments indicate a change in the rate-limiting step with electrolyte pH from the first protonation step in acidic/neutral conditions to a later one in alkaline conditions. We also show, through a detailed analysis of the microkinetics, that a surface combination of *CO and *H is inconsistent with the measured current densities and Tafel slopes. Finally, we discuss the implications of our understanding for future mechanistic studies and catalyst design.

Broader context

Electrochemical CO_2 reduction reaction (eCO_2R) has the potential to efficiently convert electricity from renewable sources like solar and wind energy to valuable fuels and chemicals. To date, copper is the only metal catalyst that can produce high value single- and multi-carbon products with substantial faradaic efficiencies, albeit at large overpotentials. The inability to find alternative catalysts is, in part, a consequence of the ongoing debate on the exact reaction mechanism for eCO_2R on Cu electrodes. This makes catalyst screening guided by first principles studies futile. Hence, identifying the rate-limiting steps towards the various eCO_2R products is imperative for the design of viable eCO_2R electrocatalysts beyond Cu. With the goal to end the ongoing debate on the exact reaction pathways towards methane and C_{2+} products, we present a joint theoretical-experimental work combining constant potential DFT simulations, pH dependent experiments and fundamental rate theory to conclusively identify the rate limiting steps.

Introduction

The impact of fossil fuel consumption on earth's environment and climate necessitates sustainable alternatives in the production, storage and use of energy resources[1,2]. Electrocatalysis is a means to convert renewable electric power to chemicals, which are an ideal medium for long-term storage and potential building blocks for the chemical industry[1]. Electrochemical $CO_{(2)}$ reduction (e$CO_{(2)}$R) represents a prime candidate for this task, since it directly closes the industrial carbon cycle by using one of the major greenhouse gases as its input and converting it into high value fuels and chemicals[1–3]. However, this process suffers from major limitations including energy losses from large overpotentials[2], the energy demand associated with CO_2 capture[4–6] and the fact that no viable catalyst towards multi-carbon (C_{2+}) products other than Copper (Cu) based electrodes has been identified to this day. Additionally, even on Cu, which has been studied as a electrocatalyst for e$CO_{(2)}$R for decades[3,7,8], the mechanism towards multi-carbon products is still disputed. Without the determination of the crucial steps in the conversion of CO_2 towards the various products, the prediction of feasible catalysts on the basis of large-scale catalyst screening is still based on trial and error.

Several attempts have been made in recent years to identify the rate-limiting steps in the reaction pathways for $eCO_{(2)}R$ on Cu electrodes [9–18]. Here, a crucial piece of the puzzle is provided by the fact that $eCO_{(2)}R$ towards C_{2+} products is pH independent on an absolute potential scale (e.g. the standard hydrogen electrode, SHE), as already shown in the seminal work of Hori et al.[7,8]. This observation vastly narrows the possible elementary step that can be rate-limiting in the production of C_{2+} products as it likely constitutes a step that does not involve a proton transfer.

Several studies have hypothesized the rate-limiting step in the production of C_{2+} products to be the first elementary step involving the dimerization of *CO to form the *OCCO species, which does not involve a proton transfer and is therefore pH-independent [11,19–22]. Alternative mechanisms based on the coupling of reaction intermediates in the later steps of the reaction have also been proposed [23–27]. When we consider the reaction kinetics (*vide infra*), we find that it is not possible to unequivocally exclude the involvement of a proton transfer in the rate-limiting step without pH-dependent activity studies performed in acidic conditions with sufficient concentration of proton donors other than H_2O, e.g. hydronium (H_3O^+) or buffering anions[18,28]. As outlined in the upper panel of Figure 1, under conditions where H_2O is the proton donor, and with the high Tafel slopes that are generally observed in experiments[18,29,30], there are three rate-limiting elementary steps that could satisfy the experimentally observed pH independence mentioned above (cf. Figure 1, C_{2+} pathways): (1) the coupling of 2 *CO molecules to form the *OCCO dimer species[11,20–22], (2) the protonation of the *OCCO dimer to *OCCOH [18], and (3) the rate-limiting protonation of *CO to *COH/*CHO followed by the coupling with *CO in a later elementary step along the reaction pathway[23–27].

Similarly, the $eCO_{(2)}R$ reaction mechanism towards methane (CH_4) has been investigated in several theoretical[9,13,31–35] and experimental studies[7,29,36–41]. The experimental studies show a reduction in the CH_4 partial current density at a given electrode potential on the SHE scale with increasing electrolyte pH (i.e. it is pH dependent). This observation suggests that the mechanism for CH_4 production deviates substantially from the C_{2+} pathway already before the first proton transfer, as otherwise the two pathways will not exhibit a different pH dependence. The challenge for this reaction lies in identifying the actual reaction pathway, given the various possibilities that exist even in the early stages of the mechanism, as outlined in the lower panel of Figure 1 (C_1 pathways). For example, the protonation of *CO to form *CHO/*COH as possible reaction intermediates in the first elementary step leads to substantially deviating possibilities for the reaction pathway towards CH_4. Additionally, the possibility of surface hydrogenation of *CO following a Langmuir-Hinshelwood type mechanism has also been proposed in recent studies [42,43]. Overall, there are many possibilities for the mechanism of $eCO_{(2)}R$ towards the various products and the actual pathways towards the various products need to be narrowed down in order to enable the search for improved electrocatalysts in e.g. theoretical screening studies.
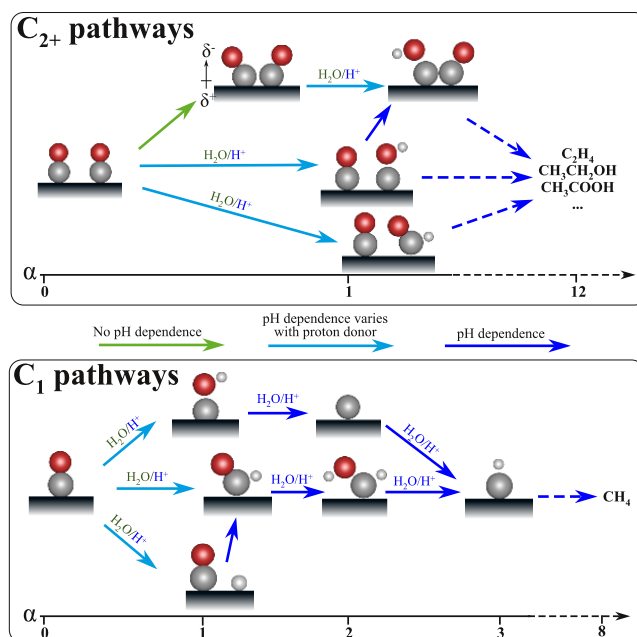

Figure 1: Schematic of the possible reaction mechanisms towards the production of C_{2+} products and CH_4 during electrochemical CO reduction on Cu. The colors of the arrows indicate the varying pH dependence in the case of the respective step being the rate-limiting step of the reaction. Note that the charge transfer co-efficient (α) can deviate from integer values for the reaction intermediates as a consequence of the non-zero surface dipole, as discussed in detail in the text.

In this article, we present a joint experimental and theoretical effort to identify the rate-limiting steps towards C_{2+} products and CH_4 by investigating the effect of the electrolyte pH during electrochemical CO reduction (COR) on polycrystalline Cu electrodes. We first give an overview of the features of generic Tafel plots associated with multi-step reduction reactions with water (H_2O) and hydronium ions (H_3O^+) as proton donors. Next, we discuss the reaction mechanisms for COR towards C_{2+} products both from an experimental and theoretical perspective: by performing pH-dependent measurements under acidic (pH 3), neutral (pH 7) and alkaline (pH 13) conditions, we can directly distinguish between the involvement of a proton-coupled electron transfer (PCET) vs. the dimerization of *CO in the rate-limiting step of COR towards C_{2+} products. We find that, even at pH 3 where there is sufficient concentration of H_3O^+ and/or buffer species to be viable proton donor(s), the measured current densities towards C_{2+} products are independent of the electrolyte pH on an SHE scale, indicating that a proton transfer is not involved in the rate-limiting step of the reaction pathway. We underscore the need for experiments in acidic conditions to exlude the involvement of a proton transfer in the rate-limiting step, as e.g. performed recently for single atom catalysts[44,45]. Potential-dependent *ab-initio* kinetics involving grand-canonical DFT simulations [46] identify that the dimerization of *CO is favored over its initial protonation to *COH/*CHO, and the potential response of *CO dimerization alone can explain the experimentally observed Tafel slopes, which is a direct consequence of the large degree

of polarization of the *OCCO dimer species. The subsequent protonation of the *OCCO dimer, on the other hand, leads to Tafel slopes which are substantially lower than the measured values, further supporting the assignment of *CO dimerization as the rate-limiting step towards C_{2+} products at all investigated pH values.

In contrast to the observations for C_{2+} products, we identify a change in the rate-limiting step with a change in the electrolyte pH and proton donor in the COR reaction pathway towards CH_4. The mechanism exhibits pH dependent activity only for pH values > 9. This behavior is a consequence of a change in the rate-limiting step from the first PCET step to the third PCET step in the reaction pathway with increasing electrolyte pH, which is further validated by our *ab-initio* kinetics studies. Simulations also identify stepped surfaces of Cu to be the most active facets for this reaction, where it proceeds via the *CHO intermediate. Based on a series of qualitative disagreements with experimental observations, we exclude surface hydrogenation in the reaction mechanism towards CH_4.

We believe that the in-depth mechanistic study of the reaction mechanism of $CO_{(2)}R$ and the effects of electrolyte pH on multi-step electrochemical reactions presented in this work will provide important descriptors and guidelines for the search for improved Cu-catalyst morphologies or alternatives to Cu in catalyst screening studies for the production of electrofuels.

Theoretical background

The Tafel slopes and pH-dependence of multi-step reduction reactions

In what follows, we describe the impact of pH and potential on the reaction rates (and current densities) of multi-step electrochemical reduction reactions where H_2O and H_3O^+ are proton donors, which allows us to perform a mechanistic analysis of the pathways for COR towards CH_4 and C_{2+} products on Cu. We first discuss qualitatively the schematics of Tafel plots for several representative examples of elementary steps and multi-step reaction mechanisms, then derive quantitatively the effects of pH and potential on rates from a rate-limiting analysis of the kinetics. Note that we do not explicitly consider the impact of buffers in this analysis. Buffers may act as proton donors directly or alter the pH[47]. If either of these two scenarios are at play, there would be a difference in activity (on the SHE scale) vs. the case where H_2O is the proton donor, by extension of the arguments we make below.

Figure 2 shows the effects of pH and U_{SHE} on Tafel plots for reduction reactions. In the top panel (I), we consider three types of single elementary steps. We show the variations in the corresponding current density (j) with respect to variations in both pH and U_{SHE}. We consider three possibilities: (i) a potential sensitive chemical reaction (as exemplified by the *CO dimerization step), and PCET steps in (ii) neutral/alkaline and (iii) acidic conditions, with H_2O and H_3O^+ as the respective proton donors. Note that in case (i), the electrolyte pH has no effect on j, since H_3O^+/OH^- species are not involved in the elementary step. Such steps show only a dependence on U_{SHE}. Similarly, if H_2O were a proton donor in a PCET step (case ii), the

chemical potential of H_3O^+ or OH^- has no effect on the initial or transition states and therefore pH has no effect on the measured current densities. However, as we will show in panel II and III below, since the final state of the reaction is dependent on pH via the activity of OH^-, any rate limiting step following an elementary step of case (II) would lead to pH dependence, in contrast to case (I).

If H_3O^+ is the proton donor in a PCET step (case iii), its activity affects the free energy of the initial state and therefore corresponding activation energy, such that the rate (and measured j) decreases with increasing pH.

This behavior extends to multi-step reactions, as illustrated in Panels (II) and (III) in Figure 2. These panels show the pH and U_{SHE} dependences corresponding to generic mechanisms with multiple PCETs (Panel III a) and with an initial potential sensitive surface reaction, followed by PCETs (Panel III b). The left and right sides of these panels show the cases where H_2O and H_3O^+ are the proton donor, respectively. In panel II, we also show the corresponding generic free energy diagram. Here, note that both a decrease in potential (U_{SHE}) and pH can shift the rate limiting step (RLS, indicated by the point on the FED with highest free energy) from a later to an earlier elementary step. These shifts in RLS give rise to increasing Tafel slopes with decreasing U_{SHE}, which are illustrated in all the Tafel plots in panel III.

Under high overpotentials (regions of the most negative U_{SHE}), the RLS shifts to the first elementary step, which results in the pH dependence shown in panel I. At lower overpotentials (more positive U_{SHE}), the RLS shift to the second step. Consider the left side of panel III(a): Here, even though H_2O is the proton donor, there is a dependence of j on pH. This pH dependence arises from the pH-dependence (a Nernstian shift) in the coverage of the intermediate involved in the RLS. It persists until the RLS shifts to the first step due to an increase in overpotential or a saturation of the intermediate's coverage, e.g. if the formation of the intermediate is exergonic, the pH dependence disappears.

When H_3O^+ is the proton donor (cf. right side of Panel I and III in Fig. 2), its activity affects the free energy of the first elementary step, as well as the RLS, thus leads to twice the effect of pH on j, compared to H_2O as the proton donor.
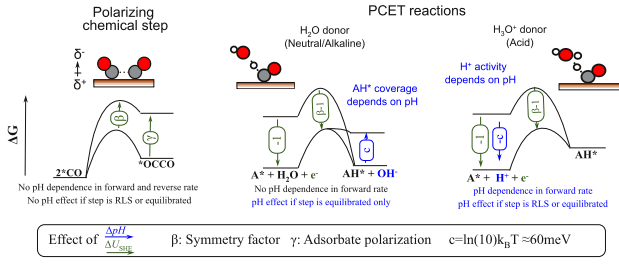
In the case of a multi-step mechanism consisting of a polarizing chemical step followed by PCETs (Panel III b), the pH dependence manifests at potential ranges where the RLS is located after or at the first PCET for the cases where H_2O and H_3O^+ are the proton donors, respectively.

Now, we show the derivations of the pH and potential dependence of multi-step electrochemical reactions from quantitative thermodynamic considerations. In general, the dependence of electrochemical reactions on the applied potential U and pH are given by an effective Arrhenius expression
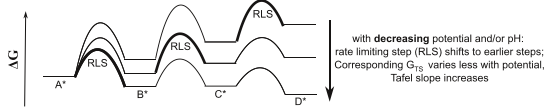
$$r(U,pH) = k_0 \exp\left(-\frac{\Delta G^{\ddagger}(U,pH)}{k_B T}\right), \qquad (1)$$

where $r(U,pH)$ is the rate of the reaction, k_0 refers to the product of the attempt frequency ($\frac{k_B T}{h}$) and the concentration of the reactants in the chosen standard state (denoted by the

I. pH dependence of elementary steps

Polarizing chemical step

PCET reactions

H₂O donor (Neutral/Alkaline)

H₃O⁺ donor (Acid)

δ^-
δ^+

AH* coverage depends on pH

H⁺ activity depends on pH

ΔG

2*CO   *OCCO

A* + H₂O + e⁻   AH* + OH⁻

A* + H⁺ + e⁻   AH*

No pH dependence in forward and reverse rate
No pH effect if step is RLS or equilibrated

No pH dependence in forward rate
pH effect if step is equilibrated only

pH dependence in forward rate
pH effect if step is RLS or equilibrated

Effect of $\frac{\Delta pH}{\Delta U_{SHE}}$ β: Symmetry factor   γ: Adsorbate polarization   c=ln(10)k_BT ≈60meV

II. Energetics of multistep reductions

RLS
RLS
RLS

ΔG

A*   B*   C*   D*

with **decreasing** potential and/or pH:
rate limiting step (RLS) shifts to earlier steps;
Corresponding G_{TS} varies less with potential,
Tafel slope increases

III. Currents of multistep reductions

(a) PCETs only

Neutral/Alkaline

Acid

rate limiting step:

*CHO coverage depends on pH
*CHOH coverage depends on pH

H⁺ activity depends on pH

H⁺ activity & *CHO coverage depend on pH

H⁺ activity and *CHOH coverage depend on pH

$\log j$

>60mV/dec   <60mV/dec   <30mV/dec

Increasing overpotential

U_{SHE}

(b) Initial potential sensitive surface reaction

Neutral/Alkaline

Acid

rate limiting step:

δ^-
δ^+

*CCO coverage depends on pH

H⁺ activity depends on pH

H⁺ activity & *CCO coverage depend on pH

$\log j$

>60mV/dec   <60mV/dec   <30mV/dec
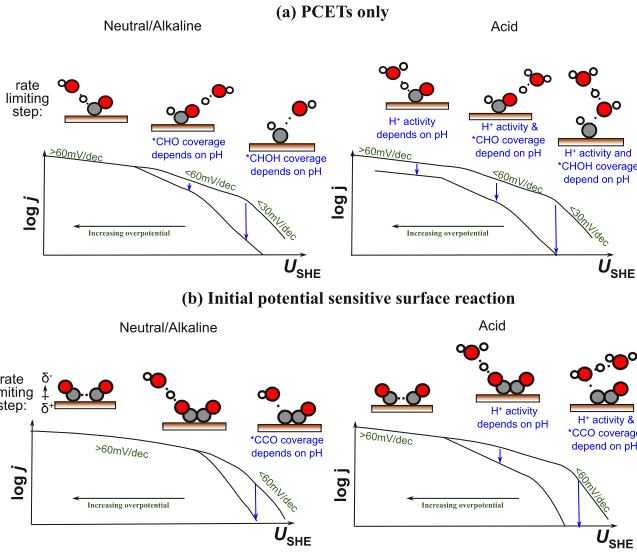
Increasing overpotential

U_{SHE}

Figure 2: Schematic illustration of the influence of the potential, U_{SHE} (green) and electrolyte pH (blue) on the reaction energetics and measured current densities of elementary steps (panel I) and multistep reaction processes (Panels II and III). In addition to the qualitative behavior, panel I shows the quantitative changes in free energy with potential (green arrows) and pH (blue arrows) given as the coefficients to ΔU_{SHE} and ΔpH. Panel II, the extension of panel I to multistep reactions, emphasizes the qualitative influence of U_{SHE} and pH on the reaction energetics and the RLS. In panel III, the qualitative pH dependence of the current density and changes in the Tafel slope upon varying the potential are depicted. Here, we distinguish between a pure PCET driven process (panel III a) and a process including a potential sensitive surface reaction (panel III b). The respective RLS at a given U_{SHE} is given in the illustrations above the qualitative polarization curves.

subscript 0), T refers to the temperature and k$_B$ represents the Boltzmann constant. $\Delta G^{\ddagger}(U, pH)$ represents the effective activation free energy of the reaction and may be dependent on the applied potential, the pH, activities of reactants, as well as temperature and pressure. Given the exponential dependence of the current on $\Delta G^{\ddagger}$, we usually work with the rate on a logarithmic scale, i.e. with the corresponding Tafel equation:

$$\log_{10} r = \log_{10} k_0 - \frac{\Delta G^{\ddagger}(U, pH)}{\ln(10)k_B T}. \qquad (2)$$

Here, all of the quantities are constants with respect to pH and potential except for $\Delta G^{\ddagger}$. The origin of the Tafel slope is, therefore, due to the dependence of $\Delta G^{\ddagger}$ on U. However, we note that the pH can have an indirect influence on the Tafel slopes: for instance, by changing the rate-limiting step and the proton donor along the reaction pathway.

Based on the chosen potential scale, varying definitions can be applied for $\Delta G^{\ddagger}$. On a purely electronic scale (e.g. SHE), $\Delta G^{\ddagger}$ can be defined by combining the thermodynamic contributions up to the RLS and the activation free energy of the RLS:

$$\Delta G^{\ddagger} = \underbrace{\sum^{N_H} \Delta G_{0,i} - N_H(\mu_e + \mu_p) - \gamma\mu_e}_{Thermodynamics} + \underbrace{\Delta G^{\ddagger}_{0,RLS} - \beta\mu_e - \mu_p}_{Kinetics}. \quad (3)$$

Here, $\Delta G_{0,i}$ and $\Delta G^{\ddagger}_{0,RLS}$ refer to the free energy of reaction of the N_H PCET reactions i up to the RLS and the reaction barrier of the RLS, respectively, where the subscript 0 refers to a well-defined electrochemical standard state which we choose as U = 0V$_{SHE}$ and pH = 0. The electronic effect on $\Delta G^{\ddagger}$, which arises from the applied potential, is included in the chemical potential of the electrons with respect to this reference state $\mu_e = -eU_{SHE}$, and the effect of pH arises from the (entropic) change of the chemical potential of the reacting protons (H₃O⁺,p) and hydroxide ions (OH⁻) $\mu_p = -\mu_{OH} = -\ln(10)k_B TpH$ with the electrolyte pH with respect to pH=0 (Note that although μ_e and μ_p are changes in chemical potential with respect to the standard state, we omitted the Δ for clarity). Both the electronic and proton chemical potentials contribute nearly equally to the *thermodynamics*, which lead to the huge success of the computational hydrogen electrode (CHE) model[48]. The influence of μ_p on *kinetics*, on the other hand is only present in acidic conditions, as indicated again in Eq. (3) by the light blue color and shown in the top panel of Figure 2, since only in such a case the proton is a reactant in the RLS.

Three coefficients in equation (3) determine the magnitude of the influence of a change in potential and pH on $\Delta G^{\ddagger}$: N_H: the number of proton transfers from the electrolyte (or PCET steps) preceding the RLS; γ : the energetic response to the overpotential of the reactants in the RLS , arising from the induced dipole perpendicular to the electrode surface, and the symmetry factor β of the RLS.[49] Depending on the nature of the rate-limiting step, various combinations of N_H, γ and β exist, which affect the Tafel plots differently. We highlight three characteristic limits of these coefficients on an SHE scale below:

$N_H = 0$: No proton transfer precedes the RLS, Tafel slope> 60 mV/dec (for any $1 > \beta > 0$), pH dependence appears only when H₃O⁺ is the proton donor (i.e. in acidic conditions). An example is the formation of CO from CO_2 on Au, where the potential sensitive adsorption of CO_2 has been found to be rate limiting[28].

$\gamma = 0$: Reactants in RLS involve do not alter the surface dipole compared to the bare slab. In this case only PCET steps

contribute to the Tafel slope. HER is an example here, given the negligible surface dipole of *H[50].

$\beta = 0$: RLS is non-electrochemical (including virtually no change to the surface dipole), and coverages dictate the potential response, such as reaction steps involving surface hydrogenation. An example is the Tafel reaction of HER[50].

We can now rewrite equation 3 by splitting the pH and potential effects (and replacing μ_e, μ_p):

$$\Delta G^{\ddagger} = \sum^{N_H} \Delta G_{0,i} + \Delta G^{\ddagger}_{0,RLS}$$
$$+ (N_H + \gamma + \beta)U_{SHE}$$
$$+ (N_H + 1)\ln(10)\,k_B T pH \qquad (4)$$

Where we again highlight the pH effect only present in the acidic case (i.e. where H_3O^+ is a reactant) by a light blue color. The three contributions to the effect of the overpotential on $\Delta G^{\ddagger}$ in equation 4 are captured by the transfer coefficient $\alpha = N_H + \gamma + \beta$. α, therefore, incorporates the net potential dependence and defines the measured Tafel slopes as

$$\left(\frac{\partial \log_{10} r}{\partial U}\right)^{-1}_{pH} = \left(\frac{\partial \log_{10} r}{\partial \Delta G^{\ddagger}}\frac{\partial \Delta G^{\ddagger}}{\partial U}\right)^{-1}_{pH} = -\frac{\ln(10)k_B T}{e\alpha}. \qquad (5)$$

While N_H is an integer, both γ and β can add up continuously along the reaction pathway. Hence, α is a smooth function meaning that the resulting Tafel slopes are not limited to any characteristic ("cardinal") values such as 60 or 120mV/dec, as has also been highlighted in a recent statistical study on experimentally determined Tafel slopes[51].

Equation 4 also shows how N_H influences the pH dependence of $\Delta G^{\ddagger}$, while γ and β only affect the potential dependence:

$$\left(\frac{\partial \log_{10} r}{\partial pH}\right)_{U_{SHE}} = \left(\frac{\partial \log_{10} r}{\partial \Delta G^{\ddagger}}\frac{\partial \Delta G^{\ddagger}}{\partial pH}\right)_{U_{SHE}} = -(N_H + 1). \qquad (6)$$

Hence, the pH dependence is only affected by the number of proton transfers (N_H) before the RLS and the nature of the proton donor. In the case where H_3O^+ is the proton donor (acidic conditions), the pH effect is always increased by a factor of one with respect to the case where H_2O is the proton donor (in neutral/alkaline conditions), as indicated by the light blue color in equation (6). As a rule, for electrochemical reduction reactions, without considering specific double layer effects, the only possible effect of increasing pH at a given applied potential on an absolute potential scale (e.g. SHE) is a reduction in the current density j, since $N_H \geq 0$.

Finally, on the reversible hydrogen electrode (RHE) scale, changes in μ_p are countered by an equal and opposite change in μ_e, thus keeping the total electrochemical driving force $\mu_{pe} = \mu_e + \mu_p = -eU_{RHE} = -(eU_{SHE} + 2.3k_B T pH)$ constant. As a consequence, the potential and pH effects cannot be separated anymore. While we discuss the energetics on this potential scale in more detail in section 9 of the SI, we highlight here that, on an RHE scale, an increase in the electrolyte pH can, for a reduction process, lead to both an increase (in neutral/alkaline conditions) or a decrease (in acidic conditions) of the reaction rate.

Results

pH-dependent experiments in acidic, neutral and alkaline conditions suggest C_{2+} products are not limited by PCET

Figure 3(a) shows the measured partial current density towards all C_{2+} products on pc-Cu at a range of pH values. We observed a Tafel slope of above 60 mV/dec and in all cases little pH dependence even in acidic conditions (pH 3), where either the buffering anion species [52–54] or H_3O^+ might be viable proton donors. As shown by panels II and III in Figure 2 for multi-step mechanisms, these two observations suggest, respectively, that the rate-limiting step is 1) the first step in a multi-step mechanism and 2) it is a potential sensitive chemical step. In acidic conditions, where H_3O^+ or buffer species are viable proton donors, a rate-limiting PCET step should show an increase in the measured C_{2+} activity vs. the situation where H_2O is the proton donor (cf. Figure 2, panel II, right). In contrast, we see that the measured current density towards C_{2+} products at pH 3 shows a slight decrease compared to neutral/alkaline electrolytes which may originate from specific adsorption of buffering anions[52] thereby blocking active sites and/or competition from CH_4 production, which depletes *CO. Therefore, we conclude that a proton transfer is not involved in the RLS towards C_{2+} products, which points to CO-CO dimerization as the rate limiting step at all investigated pH values (3-13).

We note that with mass-transport limitations associated with the diffusion of protons/buffer species, it is possible that even under acidic conditions (pH 3), H_2O is the only viable proton donor (at pH 3, $c_{H+,bulk} = 10^{-3}\,M$ while $c_{water} = 55\,M$) such that PCET from H_2O to the *OCCO dimer intermediate can be the rate-limiting step. This scenario would also give rise to a high Tafel slope (> 60 mV/dec) and no effect of pH on activity amongst the measurements at different pH (cf Figure 2, panel II, left). However, the measured HER current densities for pH 3, 7 and 13 (SI section 7) do not suggest this to be the case: as expected from Fig. 2 for the case where H_3O^+ is the proton donor, the HER current density decreases with an increase in the electrolyte pH. This observation would imply that sufficient concentration of proton donors other than H_2O (i.e. H_3O^+ and/or buffer species) are available at pH 3.
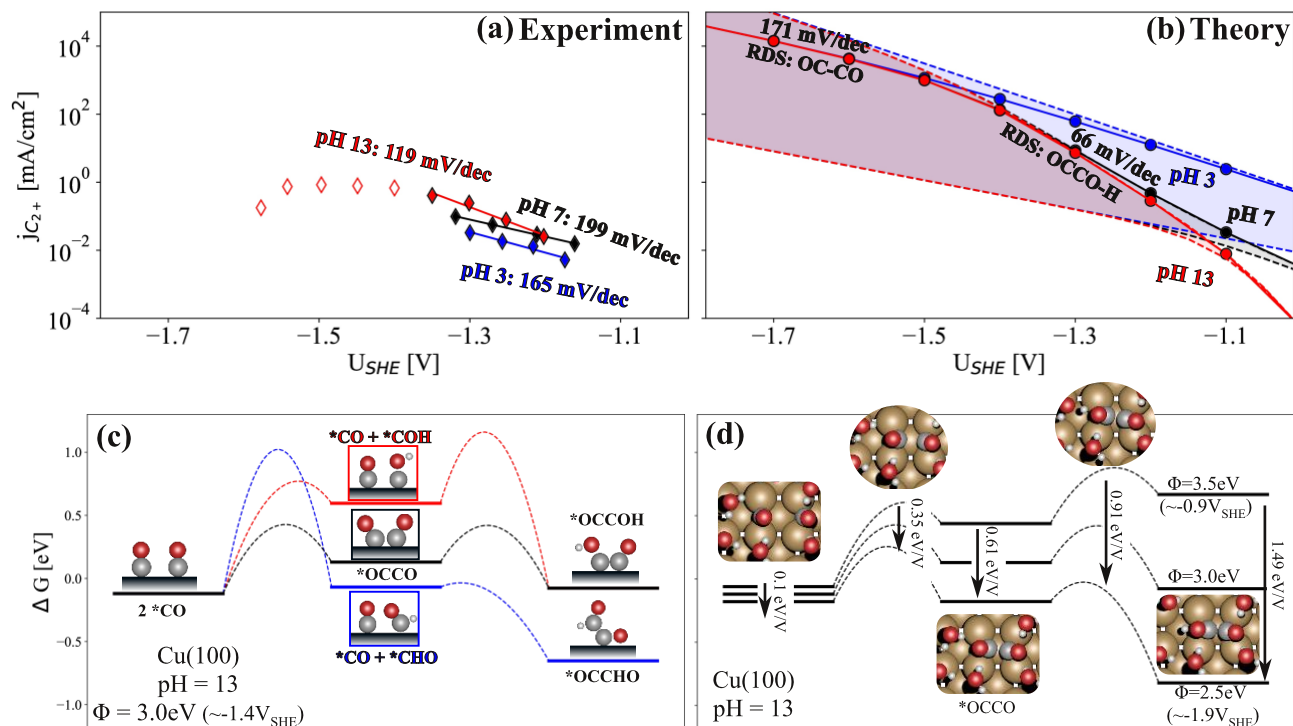
Figure 3: (a) Measured current partial densities towards C$_{2+}$ products on a polycrystalline Cu electrode. Only the filled diamonds have been used in the estimation of Tafel slopes, due to possible convolution with CO mass transport limitations at higher overpotentials. (b) Simulated current densities resulting from a microkinetic model based on the DFT calculated energetics for Cu(100). A surface fraction of 19% [81] was used in the microkinetic model. The shaded areas correspond to error estimates associated with uncertainty in the CO dimerization barrier typical for DFT (+/- 0.2eV)[62]. At all shown pHs both hydronium and H$_2$O have been considered as proton donors and the transport limitation of protons has been regarded following Ref. [82] (c) DFT calculated free energies for initial C-C coupling pathways including CO-CO coupling and the protonation of *CO to *COH/*CHO followed by coupling with *CO. In all reactions H$_2$O was considered as the proton donor. Note that although only the first two elementary steps are shown here, in the microkinetic model more subsequent steps have been included as outlined in tables S1 and S2 (d) the potential dependence of the reaction energetics along the *CO dimerization pathway computed using grand-canonical DFT simulations. In panels (c) and (d) full lines refer to thermodynamic stable states, while dashed lines represent transition state energies. The energy response to an increase in overpotential is highlighted by the arrows. The potential in both panels (c) and (d) are given in terms of the calculated work functions (ϕ). The translation from ϕ to U$_{SHE}$ in panel (b) has been made using the following relation: U$_{SHE}$ = (ϕ − 4.4 eV)/e [63]

DFT simulations and kinetic modelling suggest the formation of C$_{2+}$ products through CO dimerization is favored over a later coupling step

The predominance of the CO-CO dimerization over other coupling steps as suggested by experiment is consistent with the result of constant-potential DFT simulations based on the solvated jellium method [55] with H$_2$O as the proton donor. Figure 3(c) shows the computed free energy diagrams for CO dimerization as well as the protonation of *CO to *COH or *CHO followed by the coupling to *CO to form *OCCOH/*OCCHO on Cu(100). The 100 facet was chosen based on our finding that CO dimerization is significantly more facile on this facet compared to the 111 terrace and 211 steps and is comparable to the coupling on the 110 facet (see section 3 of the SI). We find that the *CO dimerization step followed by the protonation of *OCCO is kinetically favored over the initial protonation of *CO to *CHO/*COH. We attribute the smaller protonation barrier of *OCCO relative to *CO to the substantial polarization of the

*OCCO species. The negative charge on the oxygen atoms greatly facilitates the protonation process.

The finding that the Cu(100) and Cu(110) facets largely facilitate *CO dimerization is in line with previous theoretical[56] and experimental studies, where e.g. the application of Cu nanocubes [24,39,57,58], exhibiting predominantly 100 and 110 facets, and single crystals[8,19,59] are reported to be selective towards C$_{2+}$ products. However, we emphasize that particular care in assigning active sites is needed, given that a reconstruction of the ideal surface under reaction conditions cannot be excluded and only a small fraction of more active sites can, in principle, dominate the kinetics of the reaction[60,61].

Figure 3(d) shows the potential dependence of the free energies of the reaction steps involved in the *CO dimerization pathway, and Figure 3(b) the simulated current densities from corresponding microkinetic models at various pH values. We note that the computations suggest that at low overpotentials, *OCCOH formation would be rate limiting (i.e. the

corresponding transition state energy is the highest point in the free energy diagram). At lower (more reducing) potentials, the *CO dimerization step is rate-limiting. This change in rate-limiting step is reflected in the increase in the simulated Tafel slope with more reducing potentials akin to the schematic in Figure 2 (panel III). Note that although Figure 3(c) and (d) only show the free energies of the first two elementary steps, in the microkinetic model of panel (b) more subsequent reaction barriers and thermodynamics up to the ketene intermediate (*H2CCO) have been included, as outlined in tables S1 and S2. The transition state of *CO dimerization shows a potential dependence of 0.35 eV/V, as a consequence of the buildup of a surface dipole during the dimerization. This potential response translates into an effective transfer coefficient (α) of the same value, resulting in the computed Tafel slope of 171 mV/dec from equation 5. For the *OCCO intermediate, we found a stabilization γ of 0.61 eV/V with the applied potential. This response to the potential is also incorporated in the subsequent transition state for the protonation of *OCCO which we found to have a symmetry factor (β) of 0.3 eV/V and, hence, an overall stabilization ($\beta + \gamma$) of 0.91 eV/V. The corresponding Tafel slope for this protonation step is 66 mV/dec. Based on this qualitative analysis on the potential response of the respective reaction steps, we can already deduce that the protonation of *OCCO is not likely to be the RLS, since it would lead to Tafel slopes well below the values measured in experiments (ca. 120-200 mV/dec).

Using a microkinetic model, the calculated reaction energetics translate to the simulated current densities shown in Figure 3(b). For pH 7 and 13, where H_2O dominates as the proton donor, the protonation of *OCCO to *OCCOH is the RLS for $U < -1.4 V_{SHE}$, resulting in the computed Tafel slope of 66 mV/dec. At increased overpotentials, the RLS changes to *CO dimerization with a concomitant increase in the Tafel slope to 171 mV/dec. For pH 3, on the other hand, where H_3O^+ is the predominant proton donor, CO-CO dimerization is the RLS throughout the considered potential range, as a consequence of the spontaneous (activationless) protonation of *OCCO in our acidic transition state simulations. We emphasize here that we have not considered buffer species as proton donors in our simulations, which would also lead to differences in activity at different pH (e.g. for the experiments at pH 3 and pH 7 which involve buffering anions), in the potential region where *OCCOH formation involving a proton transfer to the *OCCO dimer is the rate-limiting step.

While our simulations show qualitative agreement with experiments at reducing potentials negative of -1.4 V_{SHE}, it is important to note that quantitative differences between experimental and theoretical kinetics at lower overpotentials can arise from several sources. Typical DFT errors for surface reaction energetics are 0.15 eV [62], but in computational electrochemistry this uncertainty is compounded by several other contributions. Firstly, we convert the workfunction (ϕ) from our ab initio constant potential simulations to a potential vs. the SHE scale (V_{SHE}) using work function for SHE determined by Trassati from experiments ($\phi_{SHE} = 4.4\ eV$)[63], and not an internal, computed ϕ_{SHE} reference from our model.

Additionally, the computational model used in this work for calculating the reaction energetics is a simplified model of the electrode-electrolyte interface. First, the static water layer that was used in our simulations might substantially reduce the degrees of freedom of H_2O molecules, and does not correspond to the (dynamic) electrode-electrolyte interface present under experimental conditions[64]. The presence of this static water layer might also alter the effective capacitance of the interface, which affects the potential dependence of the resulting reaction energetics, and in turn the simulated tafel slopes [65]. Second, no explicit ions have been used in the determination of the reaction barriers, hence we do not include any local interactions between ions and transition states that could potentially be present at the electrode-electrolyte interface. [66] Finally, the calculation of electrochemical barriers on the basis of grand-canonical DFT with a combination of implicit and explicit solvation is still a fairly new concept and further improvements and shortcomings of these methods have already been pointed out in previous work[65,67,68].

From an experimental standpoint, several factors might convolute analysis of the intrinsic reaction kinetics, including mass transport limitations of the reactant species (e.g., CO and the proton donors), the detection sensitivities for product analysis, and deactivation/dynamic changes of the surface active-sites. We observed a small diffusion-limited CO reduction partial current density (< 1 mA cm^{-2}) due to the extremely low solubility of CO in aqueous electrolyte (~ 1 mM under our testing conditions[69]) and the relatively thick boundary layer (~80 ⏶m[70]) of our electrochemical cell. In addition, the partial current densities (or activity) of CO reduction are obtained based on *ex situ* analytical methods (i.e., GC and NMR), that provide averaged values from electrolysis time scales of tens of minutes. Therefore, these data cannot fully represent the true kinetics at the electrode/electrolyte interface unless the system is continuously under steady-state conditions, which is rarely the case. In fact, Cu-based electrodes can undergo dynamic changes in morphology[21,71], surface faceting[72] and oxidation states[73] that affect the reaction kinetics. Thus, we suggest the development of new product analysis strategies that enable the collection of more accurate kinetic data with improved temporal resolution will strengthen correlations between experiment and theory[74–76].

In order to illustrate the sensitivity of the simulated current density and Tafel slopes, we also added error estimates in Figure 3(b), represented by the shaded regions. In these regions the *CO dimerization barrier was varied by +/- 0.2 eV. This analysis shows that an increase of the *CO dimerization barrier by 0.2 eV already leads to a three orders of magnitude reduction in the simulated current density towards C$_{2+}$ products and a Tafel slope corresponding to the *CO dimerization step being rate-limiting throughout the experimentally investigated potential region. These observations highlight the sensitivity of the mechanism (and simulations in general) to the computed reaction energetics. Hence, we emphasize that the main finding from our theoretical analysis is that a C$_2$ pathway with C-C coupling through *CO dimerization is preferred over pathways involving later coupling steps between protonated

intermediates. Furthermore, the *CO dimerization step exhibits a significant potential response, consistent with the measured Tafel slopes.

Experiments suggest a change in the rate-limiting step with varying pH for CH₄ production

Figure 4(a) shows the measured partial current densities towards methane at pH 3, 7 and 13, which in contrast to C_{2+} products, exhibit pH dependent activity and smaller Tafel slopes (43-89 mV/dec) with increasing pH, and a decrease in these Tafel slopes with respect to U_{SHE}. These different features suggest that the mechanism for methane production differs fundamentally from the C_{2+} pathway. We find a Tafel slope of 43 mV/dec at pH 13 , which suggests that the second step is rate limiting (N_H > 0, cf. Eq. 3 and the scheme shown in Figure 2 (II)). This hypothesis was already put forth by Hori et al [7,8]. We note that if CO transport limitations are present at such negative potentials, the corresponding intrinsic Tafel slope would be even smaller, which would still imply that a later step is rate limiting. At lower pH values of 3 and 7, the Tafel slope is above 80 mV/dec, which suggests that the RLS is the first PCET step (N_H = 0). The measured current densities do not overlap for these two pH values on the SHE scale, which indicates that the proton donor is different in the two measurements. At pH 7, only water and buffer species are viable proton donors, while at pH 3, H_3O^+ species might also be a viable proton donor.

Based on the above observations of the dependence of activity on U_{SHE} and pH, there are two possibilities for the mechanism towards CH₄:

Mechanism-I: a purely *electrochemical* process consisting of an initial PCET towards *CO to form *CHO/*COH, followed by the subsequent PCET steps towards CH₄ (cf. Figure 1). At pH 13, where the Tafel slope <60mV/dec, a later step in the pathway would be rate limiting (N_H>0), which leads to a smaller Tafel slope and a distinct pH dependence. As suggested in the panel II of Figure 2 a smaller pH could give rise to a shift in the RLS to the first protonation step of *CO, where no pH dependence is expected (N_H=0) except in the case of a change in proton donor that leads to a change in the activation energy $\Delta G_{0,RLS}^{\ddagger}$ for the proton transfer.

Mechanism-II: the *surface hydrogenation* of *CO is rate-limiting step as has been discussed in previous studies [42,43]. Since surface hydrogenations are chemical processes that are largely insensitive to changes in the applied potential, a finite Tafel slope can only arise from a change in *H coverage at high pH, which in the Nernstian limit would give rise to slopes close to 60 mV/dec, as described in more detail in section 6 of the SI. In this scenario, the rate-limiting step would be the hydrogen adsorption (Volmer) step at neutral and acidic pH.

DFT calculated energetics suggest a purely electrochemical mechanism towards CH₄

We performed grand-canonical DFT and microkinetic simulations for both mechanisms (I and II) towards CH₄ on four Cu facets: 111, 100, 110 and 211 (see also SI section 2 for computational details). As we show in section 4 of the SI, following Mechanism-I, all four facets show considerable pH
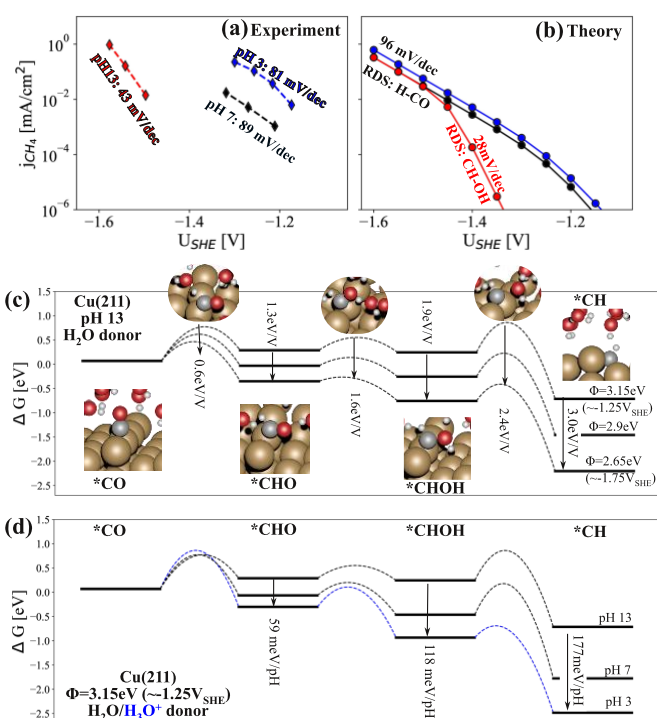

Figure 4: (a) Measured current densities towards CH₄ on Cu-foil for pH 3, 7 and 13. (b) Simulated current densities resulting from a microkinetic model using the DFT reaction energetics for the Cu(211) facet. A surface fraction of 5% was assumed for the 211 facet [34]. (c) Free energy diagram for Cu(211) towards CH₄ at varying workfunctions (a link to the experimental SHE potential scale can be made using the relation: $U_{SHE} = (\phi − 4.4 \text{ eV})/e$). (d) Free energy diagram for the reaction pathway towards CH₄ at varying electrolyte pH. For pH 7 and 13, the reaction kinetics are simulated with H_2O is the proton donor, while the kinetic simulations at pH 3 were performed with H_3O^+ as the proton donor.

dependence towards methane at high electrolyte pH, since the rate-limiting step is later than the first protonation step (N_H > 1).

On the 111, 110 and 211 facets, the barrier towards *CHO is lower than towards *COH. For the pathway via *CHO on the 211 facet, identified as most active and shown in Figure 4(b-d), the desorption of OH^- from the *CHOH intermediate is limiting at low overpotentials (> $1.5V_{SHE}$ at pH 13) and/or high electrolyte pH (> pH 9), while the protonation of *CO to *CHO is limiting at higher overpotentials and/or low pH. The direct switch in the rate-limiting step from the first to the third elementary step arises from the facile protonation of the *CHO intermediate in the second elementary step (cf. Figure 1, C_1 pathways). We attribute the facility of this step to the configuration of *CHO, which has its O atom openly accessible to the proton donor, as well as its polarization ($\gamma_{*CHO} \approx 0.3$), as has been observed by Liu et al.[18].

On the 100 facet, the barrier towards *COH is lower than that of *CHO, and at low overpotentials and/or high pH, the rate-limiting step is *COH -> *C (cf. Figure S2, S3). This is a consequence of the endergonic thermodynamics of the
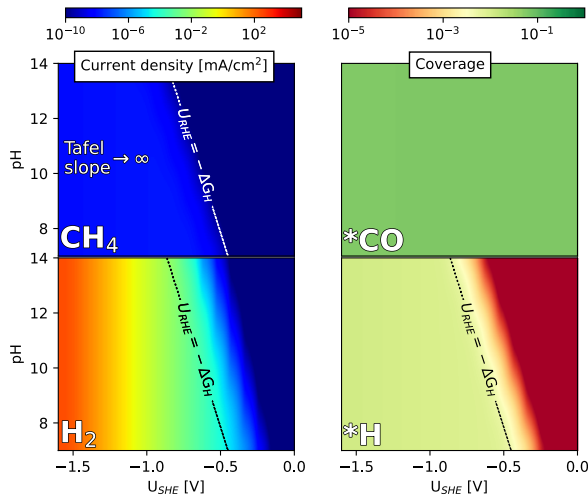
Figure 5: Simulated current densities (j) for CH$_4$ and H$_2$ (left) and coverages for *CO and *H (right) obtained from a microkinetic model for mechanism II towards CH$_4$ on Cu(211. The rate-limiting step for this pathway is the surface hydrogenation of *CO to *CHO. All the reaction energetics used in the microkinetic model have been calculated with DFT with the only exception being the reaction barrier of the hydrogen liberation (Heyrovsky) step in HER, which was adapted in order to create a non-zero hydrogen coverage. In this example, an equal symmetry factor (β = 0.36 eV/V) has been chosen for the Volmer and Heyrovsky steps, as has been calculated for the Volmer step. A detailed analysis of the effects of varying symmetry factors is provided in the section 6 of the SI.

protonation of *CO combined with the low reverse barrier (i.e. the deprotonation of *COH) of this step. Again, in this case, at high overpotentials we find that the rate-limiting step is shifted to the first elementary step, *CO -> *COH.

Since the Cu(211) facet exhibits the highest activity in our simulations, we suggest that steps are most likely the active sites for CH$_4$ production. We show the free energy diagrams and the corresponding simulated current densities obtained from a microkinetic model for the CH$_4$ pathway in Figure 4(b-d). We find a reasonable qualitative agreement with the experimentally measured partial current densities towards CH$_4$ (cf. Figure 4(a)), given that no *post-hoc* corrections were applied to the computed free energies. As mentioned above, the third step in the reaction pathway is rate-limiting at low overpotentials as can be seen in the free energy diagram at ϕ_{SHE} = 3.15 eV (~-1.25 V$_{SHE}$) in Figure 4(c) and/or high electrolyte pH (cf. the free energy diagram at in Figure 4(d)), which leads to a simulated Tafel slope of 28 mV/dec. Figure 4 (b) and (d) show that reducing the electrolyte pH results in a change in the rate-limiting step to the first protonation step (*CO->*CHO). This change in RLS corresponds to a change of N$_H$ from 2 to 0. As shown in Figure 2, Panel II and eq. 4, this early RLS, with N$_H$ =0, gives rise to pH-independent activity on the SHE scale with H$_2$O as the proton donor, as well as a larger Tafel slope (computed to be 96 mV/dec in our simulations). Upon reducing the pH below 4, the current at a given potential starts to increase again due to a change in proton donor from H$_2$O to H$_3$O$^+$. Interestingly, we find a negligible change in the Tafel slope upon changing the proton donor, which arises from the

similarity in the symmetry factor (β) of 0.62 eV/V for the protonation of *CO by H$_3$O$^+$ (pH 3) and H$_2$O (pH 7 and 13).

In contrast to the observations with Mechanism-I, the simulated current densities towards CH$_4$ obtained from a microkinetic model following Mechanism-II lead to substantial qualitative mismatch with the experimental results (cf. Figure 5, which shows the computed *j* for CH$_4$ and H$_2$ production and the coverages for *CO and *H as a function of pH and potential). Note that in these simulations, we chose to consider the surface hydrogenation of *CO to *CHO due to stronger binding of *CHO compared to *COH on all the investigated facets. We find this mechanism to be pH-dependent only at very low overpotentials. Additionally, the substantial potential response (i.e. low Tafel slopes) at high overpotential observed in experiments (Figure 4(a)) could not be reproduced with this model. Instead, H$_2$ production outcompetes CH$_4$ production due to the potential dependent second PCET step (Heyrovsky) reaction as evident by its higher current densities. We discuss the origin of this behavior with a detailed analysis in section 6 of the SI. The major takeaways from this analysis are as follows:

(1) For Mechanism-II to reproduce the experimentally observed Tafel slopes at high pH, the hydrogen coverage needs to change exponentially with the applied potential at typical working conditions (i.e. ~ -1.4 V$_{SHE}$ ≈ -0.7 V$_{RHE}$ at pH 13). The hydrogen binding free energy (ΔG_H), which varies from 0 eV to + 0.3 eV on the investigated Cu facets, determines the ranges of potential and pH where the hydrogen coverage can change exponentially, namely at potentials (U_{RHE}) more positive than -ΔG_H/e. At typical experimental conditions for COR, since the hydrogen coverage is saturated, the simulated Tafel slopes are effectively infinite (see top left panel of Figure 5).

(2) In addition to the mismatch in the potential response with experiments, the high surface hydrogenation barrier for *CO to *CHO (~1 eV) computed on all the Cu facets leads to very low simulated current densities (ca. 10^{-7} mA/cm^2) even at high overpotentials. Here it is important to note that the potential response of the surface hydrogenation of *CO is nearly negligible ($\beta \approx$ 0); i.e. it is a chemical process such that its activation energy is not altered by a change in U_{SHE}.

Based on above considerations and the simulated current densities based on the surface hydrogenation pathway, *we conclude that CH$_4$ production via Mechanism-II is unlikely*.

Discussion of results with previous measurements

In the following, we evaluate our mechanistic understanding against several previously published experimental datasets. The left panel of Figure 6 shows the electrochemically active surface area (ECSA) normalized current densities for C$_{2+}$ products vs. U_{SHE} for electrochemical CO$_2$ and CO reduction. In this analysis, we include experimental data from both CO$_2$ and CO reduction on Cu electrodes. The overlap of both CO and CO$_2$ reduction data suggests that *CO is a crucial intermediate, whose
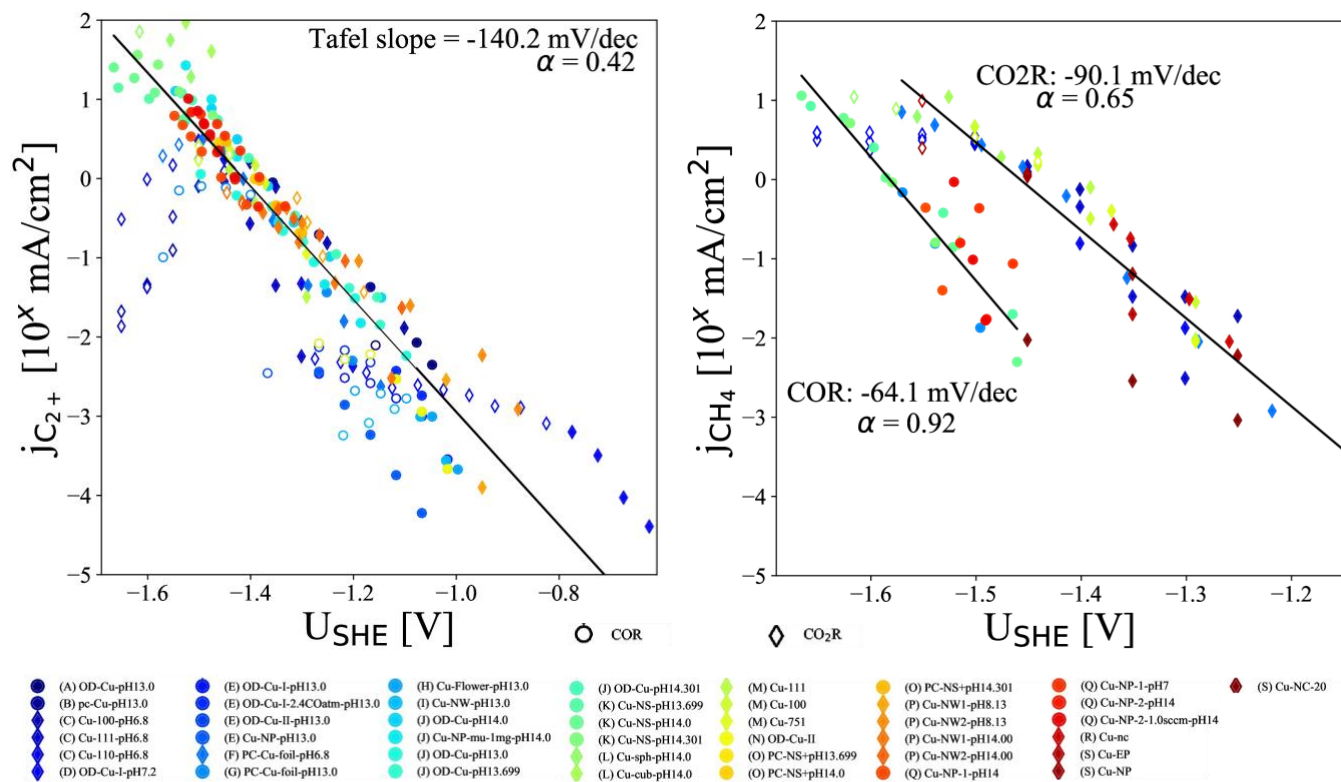
Figure 6: Tafel analysis based on a collection of experimental studies including both CO and CO_2 reduction experiments towards C_{2+} products (left) and CH_4 (right). All included current densities have been normalized with respect to the electrochemically effective surface area (ECSA). Open markers represent measurements that are possibly convoluted with mass transport and therefore have not been included in the estimation of the Tafel slopes. For methane, the partial current densities resulting from CO_2 reduction and CO reduction are marked as diamonds and circles, respectively. The individual Tafel slopes are given in the SI section 9. The respective references are: A: [83], B: [84], C: [85], D: [86], E: [79], F: [87], G:[29], H:[70], I:[88] J:[89], K:[40], L: [90], M: [91], N: [79], O:[40], P:[92], Q: [41], R: [93], S: [94]

coverage is independent of whether it is created in the reduction process (CO_2R) or directly fed in (COR). This strongly suggests that its coverage is saturated and determined by equilibration with gas phase CO, in line with the comparatively weak binding of *CO on Cu. Our simulations show the same trends: In Figure S4 we show the simulated *CO coverages. On all simulated facets the coverage is below 40%, as a consequence of the steep rise in *CO-*CO interactions at elevated coverages. Additionally, the small surface dipole created during the adsorption of *CO, leads to a negligible potential response of its coverage on the 100 and 211 facets and a minor potential response on the 111 facet (see also SI section 12 for the tabulated potential responses). The 110 facet, on the other hand showed a steep reduction in *CO coverage at higher overpotential, due to the build-up of a *CHO coverage. Consistent with the discussion above, we observe no dependence of C_{2+} activity on the electrolyte pH. A fit over all the data also gives an overall Tafel slope of ~ -140 mV/dec in reasonable agreement with the measured values reported above (cf. Figure 3a). This result further strengthens the analysis shown in Figure 3 and its conclusion that the coupling of 2 *CO molecules to form the *OCCO dimer species is the rate-limiting step for $CO_{(2)}R$ towards C_{2+} products.

Interestingly, although a wide range of nanostructured Cu surfaces and experimental setups including H-cells and gas diffusion electrodes (GDEs) are compared in the plot, the spread of the current density seems to be within an order of magnitude, as noted in previous studies [3,77]. Given that $CO_{(2)}R$ is dependent on the square of the *CO coverage on the active sites of the catalyst, this spread suggests that the number of active sites differs by less than a factor of 5. We postulate that the restructuring of copper at reaction conditions might be at play here, as the surface has been shown to be dynamic in electrochemical $CO_{(2)}R$ experiments [78].

In contrast to the Tafel plot for C_{2+} products, analyzing recently published results for methane production, shown in the right panel of Figure 6, we could clearly identify two distinct regions. These two regions, in contrast to Hori's data [7,8], are visible even if the current density is "corrected" by the electrolyte pH (see SI section 11). The first region corresponds to measurements performed with CO_2 as the reactant at pH close to 7, the second is a result of studies starting from CO, performed at higher pH values (pH ~ 13). The two regions in Figure 6 (right) show different slopes: The > 60 mV dec^{-1} Tafel slope for the measurements performed at lower pH (pH ~ 6.8) suggest the possibility of an early rate-limiting step. We note that the smaller number of data points and high degree of noise at high pH precludes as reliable a mechanistic interpretation. However, we do observe a reduction in both the mean (cf. Figure 6) and individual Tafel slopes (cf. Figure S15) and the partial current

density towards CH_4 for experiments performed in alkaline conditions (pH ~ 13) suggesting a rate-limiting step beyond the first PCET step, in agreement with the findings of the present study.

Implications for future mechanistic studies and catalyst design

Although the present pH-dependent experiments in conjunction with theoretical mechanistic studies show *CO dimerization to be the rate limiting step for C_{2+} products on Cu electrodes is conclusive, alternative experiments investigating the involvement of a proton in the rate-limiting step could still be performed. The substitution of H_2O with D_2O might lead to a measurable KIE effect for a rate-limiting step involving a proton transfer, while having little/no effect for a potential-dependent chemical rate-limiting step (i.e. *CO dimerization). However, we note that the effect might be too small for definite exclusion of one or the other mechanism[28]. Resasco *et al.* [53] recently showed that the current densities measured in strongly buffered electrolytes linearly depends on the concentration of the buffering anion. Hence, further studies on the influence of electrolyte buffers on the performance in $CO_{(2)}R$ can also provide important insights into the distinction in the nature of the rate-limiting step. Finally, experiments performed at lower overpotentials than those that have been investigated in this work might be able to observe a change in the rate-limiting step from *OCCO protonation to *CO dimerization that was predicted by our *ab-initio* kinetics simulations. We note that such a study might necessitate surfaces with high roughness factors such as oxide derived Cu (OD-Cu), [79] and/or setups with high product sensitivity in order to obtain measurable current densities at low overpotentials.

For theoretical studies, we emphasize that it is crucial to incorporate the effect of potential sensitivity due to charge reorganization (denoted in this work as γ) in simulations of multi-step electrochemical reactions. This is exemplified by the rate limiting CO dimerization step for the production of multicarbon products that exhibits a significant potential response. Additionally, we emphasize that accounting for the whole reaction process up to the rate limiting step, with the inclusion of reaction kinetics, is crucial for a benchmark of the calculated results to experimental observables, since pH and potential dependence cannot be estimated from single elementary steps. Finally, a thorough understanding of electrochemical reactions at the solid/liquid interface, in principle, would also benefit from multiscale models that account for mass transport including diffusion and migration of species.

From an experimental standpoint, we emphasize the need to develop new reactor-designs and product analyzing techniques that can enable the collection of more precise and time-resolved intrinsic kinetic data in an extended electrode potential window. More robust kinetic information can be better interpreted by theoretical models, thereby providing new insights to guide the design of more active and selective catalysts.

Based on the identified rate-determining steps for the production of methane and C_{2+} products, we are also in a position to suggest general principles for future catalyst design. Since the formation of multicarbon products is limited by *CO dimerization, the binding energy of *OCCO can serve as an important descriptor for the identification of electrode materials with high activity towards multicarbon products. Furthermore, since no proton is involved in the RLS, working in buffer free electrolytes or using buffers unable to act as proton donors (i.e. "innocent" buffers) is recommended for high C_{2+} yield[47,53]. Finally, the use of Cs^+ over other alkali-metal cations has been shown to improve $eCO_{(2)}R$ activity towards multicarbon products.[80] We attribute this behavior to the substantial dipole moment of *OCCO, similar to previous results for CO_2 reduction to CO.[28]

For methane, as we find the rate-limiting step to involve a proton transfer step, buffering anions with a lower pK_a than water can be used as proton donors (i.e. "non-innocent" buffers) to accelerate the rate limiting step for methane production.[53] Additionally, since we conclusively exclude surface hydrogenation as the rate-limiting step for methane production, the negative order in CO reported in previous studies that has been attributed to involvement of the surface hydrogenation involving *CO and *H would also need to be reconsidered.[30,42]

Conclusions

Elucidating the reaction pathways including the rate-limiting steps in electrochemical $CO_{(2)}$ reduction (eCO_2R) is challenging due to the complexity of the reaction mechanisms towards C_1 and C_{2+} products. Based on pH resolved experiments reaching down to acidic conditions, necessary to unequivocally exclude the involvement of a proton transfer in the rate-limiting step, and constant potential *ab-initio* calculations including both H_2O and H_3O^+ proton donors, we demonstrated that only a reaction whose rate is limited by the coupling of two CO molecules is able to explain the measured results for $eCO_{(2)}R$ to multicarbon products. Two independent approaches in the analysis resulted in the same result, namely the absence of a change in current density upon change in proton donor and the lower potential response to current density as compared to the protonation of *OCCO. Our analysis suggests a transition in the RLS from *CO dimerization to *OCCO protonation might be possible at low overpotentials that has not been so far observed within the potential ranges probed in the experiments.

For methane formation, we conclusively excluded a mechanism based on the surface combination of *CO and *H, since it would lead to both undetectable current densities and close to infinite Tafel slopes at reaction conditions. On the other hand, a fully electrochemical mechanism explains the experimentally observed activities. We identified a change in the rate limiting step with the electrolyte pH for methane production. While at neutral and acidic conditions the first PCET step is rate limiting, at pH > 9, the third step is rate limiting, leading to a pH dependence of the mechanism only in alkaline conditions.

Overall our analysis conclusively elucidates the rate limiting steps in eCO$_{(2)}$R towards both methane and C$_{2+}$ products. The results also suggest that electrocatalysts which stabilize the *OCCO dimer beyond Cu to be alternative candidates for the production of high value C$_2$ products.

Author contributions

Conflicts of interest

Acknowledgements

References

1   O. S. Bushuyev, P. De Luna, C. T. Dinh, L. Tao, G. Saur, J. van de Lagemaat, S. O. Kelley and E. H. Sargent, *Joule*, 2018, **2**, 825–832.

2   P. De Luna, C. Hahn, D. Higgins, S. A. Jaffer, T. F. Jaramillo and E. H. Sargent, *Science (80-.).*, 2019, **364**, eaav3506.

3   S. Nitopi, E. Bertheussen, S. B. Scott, X. Liu, A. K. Engstfeld, S. Horch, B. Seger, I. E. L. Stephens, K. Chan, C. Hahn, J. K. Nørskov, T. F. Jaramillo and I. Chorkendorff, *Chem. Rev.*, 2019, **119**, 7610–7672.

4   M. Karimi, M. Hillestad and H. F. Svendsen, *Chem. Eng. Res. Des.*, 2011, **89**, 1229–1236.

5   L. E. Øi and S. H. P. Kvam, *Energy Procedia*, 2014, **63**, 1186–1195.

6   A. Kiani, K. Jiang and P. Feron, *Front. Energy Res.*, 2020, **8**, 92.

7   Y. Hori, R. Takahashi, Y. Yoshinami and A. Murata, *J. Phys. Chem. B*, 1997, **101**, 7075–7081.

8   Y. Hori, in *Modern Aspects of Electrochemistry*, Springer New York, New York, NY, 2008, pp. 89–189.

9   K. J. P. Schouten, Y. Kwon, C. J. M. van der Ham, Z. Qin and M. T. M. Koper, *Chem. Sci.*, 2011, **2**, 1902.

10   K. J. P. Schouten, Z. Qin, E. P. Gallent and M. T. M. Koper, *J. Am. Chem. Soc.*, 2012, **134**, 9864–9867.

11   F. Calle-Vallejo and M. T. M. Koper, *Angew. Chemie Int. Ed.*, 2013, **52**, 7282–7285.

12   X. Nie, W. Luo, M. J. Janik and A. Asthagiri, *J. Catal.*, 2014, **312**, 108–122.

13   W. Luo, X. Nie, M. J. Janik and A. Asthagiri, *ACS Catal.*, 2016, **6**, 219–229.

14   A. J. Göttle and M. T. M. Koper, *Chem. Sci.*, 2017, **8**, 458–465.

15   A. J. Garza, A. T. Bell and M. Head-Gordon, *ACS Catal.*, 2018, **8**, 1490–1499.

16   A. Bagger, W. Ju, A. S. Varela, P. Strasser and J. Rossmeisl, *ACS Catal.*, 2019, **9**, 7894–7899.

17   G. Mangione, J. Huang, R. Buonsanti and C. C. Corminboeuf, *J. Phys. Chem. Lett*, 2019, **10**, 4265.

18   X. Liu, P. Schlexer, J. Xiao, Y. Ji, L. Wang, R. B. Sandberg, M. Tang, K. S. Brown, H. Peng, S. Ringe, C. Hahn, T. F. Jaramillo, J. K. Nørskov and K. Chan, *Nat. Commun.*, 2019, **10**, 1–10.

19   K. J. P. Schouten, Z. Qin, E. P. Gallent and M. T. M. Koper, *J. Am. Chem. Soc.*, 2012, **134**, 9864–9867.

20   T.-T. Zhuang, Z.-Q. Liang, A. Seifitokaldani, Y. Li, P. De Luna, T. Burdyny, F. Che, F. Meng, Y. Min, R. Quintero-Bermudez, C. T. Dinh, Y. Pang, M. Zhong, B. Zhang, J. Li, P.-N. Chen, X.-L. Zheng, H. Liang, W.-N. Ge, B.-J. Ye, D. Sinton, S.-H. Yu and E. H. Sargent, *Nat. Catal.*, 2018, **1**, 421–428.

21   X. Wang, J. F. de Araújo, W. Ju, A. Bagger, H. Schmies, S. Kühl, J. Rossmeisl and P. Strasser, *Nat. Nanotechnol.*, 2019, **14**, 1063–1070.

22   Y. Y. Birdja, E. Pérez-Gallent, M. C. Figueiredo, A. J. Göttle, F. Calle-Vallejo and M. T. M. Koper, *Nat. Energy*, 2019, **4**, 732–745.

23   A. J. Garza, A. T. Bell and M. Head-Gordon, *ACS Catal.*, 2018, **8**, 1490–1499.

24   G. Mangione, J. Huang, R. Buonsanti and C. C. Corminboeuf, *J. Phys. Chem. Lett*, 2019, **10**, 4265.

25   P. Iyengar, M. J. Kolb, J. R. Pankhurst, F. Calle-Vallejo and R. Buonsanti, *ACS Catal.*, 2021, **11**, 4456–4463.

26   J. Y. Kim, W. Park, C. Choi, G. Kim, K. M. Cho, J. Lim, S. J. Kim, A. Al-Saggaf, I. Gereige, H. Lee, W.-B. Jung, Y. Jung and H.-T. Jung, *ACS Catal.*, 2021, **11**, 5658–5665.

27   H. Peng, M. T. Tang, X. Liu, P. Schlexer Lamoureux, M. Bajdich and F. Abild-Pedersen, *Energy Environ. Sci.*, 2021, **14**, 473–482.

28   S. Ringe, C. G. Morales-Guio, L. D. Chen, M. Fields, T. F. Jaramillo, C. Hahn and K. Chan, *Nat. Commun.*, 2020, **11**, 33.

29   L. Wang, S. A. Nitopi, E. Bertheussen, M. Orazov, C. G. Morales-Guio, X. Liu, D. C. Higgins, K. Chan, J. K. Nørskov, C. Hahn and T. F. Jaramillo, *ACS Catal.*, 2018, **8**, 7445–7454.

30   J. Li, X. Chang, H. Zhang, A. S. Malkani, M. Cheng, B. Xu and Q. Lu, *Nat. Commun.*, 2021, **12**, 3264.

31   A. A. Peterson, F. Abild-Pedersen, F. Studt, J. Rossmeisl and J. K. Nørskov, *Energy Environ. Sci.*, 2010, **3**, 1311.

32   X. Nie, W. Luo, M. J. Janik and A. Asthagiri, *J. Catal.*, 2014, **312**, 108–122.

33   J. D. Goodpaster, A. T. Bell and M. Head-Gordon, *J. Phys. Chem. Lett.*, 2016, **7**, 1471–1477.

34   X. Liu, J. Xiao, H. Peng, X. Hong, K. Chan and J. K. Nørskov, *Nat. Commun.*, 2017, **8**, 15438.

35   H. Xiao, T. Cheng and W. A. Goddard, *J. Am. Chem. Soc.*, 2017, **139**, 130–136.

36   M. Gattrell, N. Gupta and A. Co, *J. Electroanal. Chem.*, 2006, **594**, 1–19.

37   W. Tang, A. A. Peterson, A. S. Varela, Z. P. Jovanov, L. Bech,

W. J. Durand, S. Dahl, J. K. Nørskov and I. Chorkendorff, *Phys. Chem. Chem. Phys*, 2012, **14**, 76–81.

38   E. Laborda, M. C. Henstridge and R. G. Compton, *J. Electroanal. Chem.*, 2012, **681**, 96–102.

39   W. Luo, W. Xie, R. Mutschler, E. Oveisi, G. L. De Gregorio, R. Buonsanti and A. Züttel, *ACS Catal.*, 2018, **8**, 6571–6581.

40   W. Luc, X. Fu, J. Shi, J.-J. Lv, M. Jouny, B. H. Ko, Y. Xu, Q. Tu, X. Hu, J. Wu, Q. Yue, Y. Liu, F. Jiao and Y. Kang, *Nat. Catal.*, 2019, **2**, 423–430.

41   D. S. Ripatti, T. R. Veltman and M. W. Kanan, *Joule*, 2019, **3**, 2581.

42   M. Schreier, Y. Yoon, M. N. Jackson and Y. Surendranath, *Angew. Chemie Int. Ed.*, 2018, **57**, 10221–10225.

43   J. Li, K. Chang, H. Zhang, M. He, W. A. Goddard, J. G. Chen, M. J. Cheng and Q. Lu, *ACS Catal.*, 2019, **9**, 4709–4718.

44   A. S. Varela, M. Kroschel, N. D. Leonard, W. Ju, J. Steinberg, A. Bagger, J. Rossmeisl and P. Strasser, *ACS Energy Lett*, 2018, **3**, 48.

45   S. Vijay, W. Ju, S. Brückner, P. Strasser and K. Chan, , DOI:10.26434/CHEMRXIV.14427986.V1.

46   G. Kastlunger, P. Lindgren and A. A. Peterson, *J. Phys. Chem. C*, 2018, **122**, 12771–12781.

47   M. N. Jackson, O. Jung, H. C. Lamotte and Y. Surendranath, *ACS Catal*, 2019, **9**, 2021.

48   J. K. Nørskov, J. Rossmeisl, A. Logadottir, L. Lindqvist, J. R. Kitchin, T. Bligaard and H. Jónsson, *J. Phys. Chem. B*, 2004, **108**, 17886–17892.

49   R. Guidelli, R. G. Compton, J. M. Feliu, E. Gileadi, J. Lipkowski, W. Schmickler and S. Trasatti, *Pure Appl. Chem.*, 2014, **86**, 259–262.

50   P. Lindgren, G. Kastlunger and A. A. Peterson, *ACS Catal.*, 2019, **10**, 121–128.

51   A. M. Limaye, J. S. Zeng, A. P. Willard and K. Manthiram, *Nat. Commun.*, 2021, **12**, 703.

52   B. B. Damaskin, O. A. Baturina, E. V. Stenina and L. N. Sviridova, *Electrochim. Acta*, 2001, **46**, 3083–3090.

53   J. Resasco, Y. Lum, E. Clark, J. Z. Zeledon and A. T. Bell, *ChemElectroChem*, 2018, **5**, 1064–1072.

54   A. Wuttig, J. Ryu and Y. Surendranath, *J. Phys. Chem. C*, 2021, **125**, 17042–17050.

55   G. Kastlunger, P. Lindgren and A. A. Peterson, *J. Phys. Chem. C*, 2018, **122**, 12771–12781.

56   H. Li, Y. Li, M. T. M. Koper and F. Calle-Vallejo, *J. Am. Chem. Soc.*, 2014, **136**, 15694–15701.

57   Y. Wang, H. Shen, K. J. T. Livi, D. Raciti, H. Zong, J. Gregg, M. Onadeko, Y. Wan, A. Watson and C. Wang, *Nano Lett.*, 2019, **19**, 8461–8468.

58   K. Jiang, R. B. Sandberg, A. J. Akey, X. Liu, D. C. Bell, J. K. Nørskov, K. Chan and H. Wang, *Nat. Catal.*, 2018, **1**, 111–119.

59   Y. Huang, A. D. Handoko, P. Hirunsit and B. S. Yeo, *ACS Catal.*, 2017, **7**, 1749–1756.

60   V. P. Zhdanov and B. Kasemo, *Kinetics of Rapid Heterogeneous Reactions on the Nanometer Scale*, 1997, vol. 170.

61   J. K. Nørskov, T. Bligaard, B. Hvolbæk, F. Abild-Pedersen, I. Chorkendorff and C. H. Christensen, *Chem. Soc. Rev.*, 2008, **37**, 2163.

62   A. J. Medford, J. Wellendorff, A. Vojvodic, F. Studt, F. Abild-Pedersen, K. W. Jacobsen, T. Bligaard and J. K. Nørskov, *Science (80-.).*, 2014, **345**, 197–200.

63   S. Trasatti, 1986, **58**, 955–966.

64   O. M. Magnussen and A. Groß, *J. Am. Chem. Soc.*, 2019, **141**, 4777–4790.

65   J. A. Gauthier, C. F. Dickens, H. H. Heenen, S. Vijay, S. Ringe and K. Chan, *J. Chem. Theory Comput.*, 2019, **15**, 6895–6906.

66   E. Pérez-Gallent, G. Marcandalli, M. C. Figueiredo, F. Calle-Vallejo and M. T. M. Koper, *J. Am. Chem. Soc.*, 2017, **139**, 16412–16419.

67   J. A. Gauthier, C. F. Dickens, S. Ringe and K. Chan, *ChemPhysChem*, 2019, **20**, 3074–3080.

68   J. A. Gauthier, S. Ringe, C. F. Dickens, A. J. Garza, A. T. Bell, M. Head-Gordon, J. K. Nørskov and K. Chan, *ACS Catal.*, 2019, **9**, 920–931.

69   U. Schmidt, *Tellus*, 1979, **31**, 68–74.

70   L. Wang, S. Nitopi, A. B. Wong, J. L. Snider, A. C. Nielander, C. G. Morales-Guio, M. Orazov, D. C. Higgins, C. Hahn and T. F. Jaramillo, *Nat. Catal.*, 2019, **2**, 702–708.

71   P. Grosse, D. Gao, F. Scholten, I. Sinev, H. Mistry and B. Roldan Cuenya, *Angew. Chemie Int. Ed.*, 2018, **57**, 6192–6197.

72   Y.-G. Kim, J. H. Baricuatro, A. Javier, J. M. Gregoire and M. P. Soriaga, *Langmuir*, 2014, **30**, 15053–15056.

73   Q. Lei, H. Zhu, K. Song, N. Wei, L. Liu, D. Zhang, J. Yin, X. Dong, K. Yao, N. Wang, X. Li, B. Davaasuren, J. Wang and Y. Han, *J. Am. Chem. Soc.*, 2020, **142**, 4213–4222.

74   E. L. Clark and A. T. Bell, *J. Am. Chem. Soc.*, 2018, **140**, 7012–7020.

75   P. Lobaccaro, L. Mandal, M. R. Motapothula, M. Sherburne, J. Martin, T. Venkatesan and J. W. Ager, *Energy Technol.*, 2018, **6**, 110–121.

76   P. Khanipour, M. Löffler, A. M. Reichert, F. T. Haase, K. J. J. Mayrhofer and I. Katsounaros, *Angew. Chemie - Int. Ed.*, 2019, **58**, 7273–7277.

77   J. Resasco and A. T. Bell, *Trends Chem.*, 2020, **2**, 825–836.

78   S. H. Lee, J. C. Lin, M. Farmand, A. T. Landers, J. T. Feaster, J. E. Avilés Acosta, J. W. Beeman, Y. Ye, J. Yano, A. Mehta, R. C. Davis, T. F. Jaramillo, C. Hahn and W. S. Drisdell, *J. Am. Chem. Soc.*, 2021, **143**, 588–592.

79   C. W. Li, J. Ciston and M. W. Kanan, *Nature*, 2014, **508**, 504–507.

80   J. Resasco, L. D. Chen, E. Clark, C. Tsai, C. Hahn, T. F. Jaramillo, K. Chan and A. T. Bell, *J. Am. Chem. Soc.*, 2017, **139**, 11277–11287.

81   R. Tran, Z. Xu, B. Radhakrishnan, D. Winston, W. Sun, K. A. Persson and S. P. Ong, *Sci. Data*, 2016, **3**, 160080.

82   P. S. Lamoureux, A. R. Singh and K. Chan, *ACS Catal.*, 2019, **9**, 6194–6201.

83   E. Bertheussen, A. Verdaguer-Casadevall, D. Ravasio, J. H. Montoya, D. B. Trimarco, C. Roy, S. Meier, J. Wendland, J. K. Nørskov, I. E. L. Stephens and I. Chorkendorff, *Angew. Chemie - Int. Ed.*, 2016, **55**, 1450–1454.

84   E. Bertheussen, T. V Hogg, Y. Abghoui, A. K. Engstfeld, I. Chorkendorff and I. E. L. Stephens, *ACS Energy Lett.*, 2018, **3**, 634–640.

85   Y. Huang, A. D. Handoko, P. Hirunsit and B. S. Yeo, *ACS Catal.*, 2017, **7**, 1749–1756.

86   C. W. Li and M. W. Kanan, *J. Am. Chem. Soc*, 2012, **134**, 7231–7234.

87   K. P. Kuhl, E. R. Cave, D. N. Abram and T. F. Jaramillo, *Energy Environ. Sci.*, 2012, **5**, 7050.

88   D. Raciti, L. Cao, K. J. T. Livi, P. F. Rottmann, X. Tang, C. Li, Z. Hicks, K. H. Bowen, K. J. Hemker, T. Mueller and C. Wang, *ACS Catal.*, 2017, **7**, 4467–4472.

89   M. Jouny, W. Luc and F. Jiao, *Nat. Catal.*, 2018, **1**, 748–755.
90   G. L. De Gregorio, T. Burdyny, A. Loiudice, P. Iyengar, W. A. Smith and R. Buonsanti, *ACS Catal.*, 2020, **10**, 4854–4862.
91   C. Hahn, T. Hatsukade, Y.-G. Kim, A. Vailionis, J. H. Baricuatro, D. C. Higgins, S. A. Nitopi, M. P. Soriaga and T. F. Jaramillo, *Proc. Natl. Acad. Sci.*, 2017, **114**, 5918–5923.
92   J. Zhang, W. Luo and A. Züttel, *J. Mater. Chem. A*, 2019, **7**, 26285–26292.
93   A. S. Varela, M. Kroschel, T. Reier and P. Strasser, *Catal. Today*, 2016, **260**, 8–13.
94   D. Ren, B. S.-H. Ang and B. S. Yeo, *ACS Catal.*, 2016, **6**, 8239–8247.